The influence of intra-cortical microstructure on the contrast in ultrasound images of the cortex of long bones: a 2D simulation study

Amadou Sall DIA, Guillaume Renaud, Aida Hejazi Nooghabi, Quentin Grimal

The influence of intra-cortical microstructure on the contrast in ultrasound images of the cortex of long bones: a 2D simulation study

Amadou Sall DIA[1a], Guillaume RENAUD[a,b], Aida Hejazi NOOGHABI[a], Quentin GRIMAL[2a]

[a] *Sorbonne Université, INSERM, CNRS, Laboratoire d'Imagerie Biomédicale, LIB, F-75006, Paris, France*
[b] *Department of Imaging Physics, Delft University of Technology, The Netherlands*

Abstract

Decreased thickness of the bone cortex due to bone loss in the course of ageing and osteoporosis is associated with reduced bone strength. Cortical thickness measurement from ultrasound images was recently demonstrated in young adults. This requires the identification of both the outer (periosteum) and inner (endosteum) surfaces of the bone cortex. However, with bone loss, the cortical porosity and the size of the vascular pores increase resulting in enhanced ultrasound scattering which may prevent the detection of the endosteum. The aim of this work was to study the influence of cortical bone microstructure variables, such as porosity and pore size, on the contrast of the endosteum in ultrasound images. We wanted to estimate the range of these variables for which ultrasound imaging of the endosteum is feasible. We generated synthetic data using a two-dimensional time-domain code to simulate the propagation of elastodynamic waves. A synthetic aperture imaging sequence with an array transducer operating at a center frequency of 2.5 MHz was used. The numerical simulations were conducted for 105 cortical microstructures obtained from high resolution X-ray computed tomography images of ex vivo bone samples with a porosity ranging from 2 to 24 %. Images were reconstructed using a delay-and-sum (DAS) algorithm with optimized f-number, correction of refraction at the periosteum, and sample-specific wave-speed. We observed a range variation of 18 dB of endosteum contrast in our data set depending on the bone microstructure. We found that as porosity increases, speckle intensity inside the bone cortex increases whereas the intensity of the signal from the endosteum decreases. Also, a microstructure with large pores (diameter $>$ 250 µm) was associated with poor endosteum visibility, compared with a microstructure with equal porosity but a more narrow distribution of pore sizes.

These findings suggest that ultrasound imaging of the bone cortex with a probe operating at a central frequency of 2.5 MHz using refraction-corrected DAS is capable of detecting the endosteum of a cortex with moderate porosity (less than about 10%) if the largest pores remain smaller than

[1]Corresponding author. E-mail address: amadou.dia@sorbonne-universite.fr

[2]Given his role as Associate Editor of this journal, Quentin GRIMAL had no involvement in the peer-review of this article and had no access to information regarding the peer-review. Full responsibility for the peer-review process for this article was delegated to another Editor of this journal.

about 200 µm.

1. Introduction

Bone fragility associated with osteoporosis and the resulting increased risk of fracture is an important medical threat as nine million fragility fractures occur annually worldwide [1]. The prediction of fracture risk is based on clinical factors and, often, areal bone mineral density (aBMD) measured with dual energy X-ray absorptiometry (DXA). However, many individuals who are at high risk of fracture are not identified with aBMD assessed with DXA [2, 3]. Quantitative ultrasound (QUS) methods to characterize trabecular and cortical bone have been developed in the past three decades to overcome the limitations of DXA and provide a non ionizing, portable, and affordable diagnostic tool for osteoporosis [4, 5].

While ultrasound imaging can accurately image the outer surface of bones [6], current clinical ultrasound scanners fail to reveal their inner structure. Only recently, with adapted image reconstruction methods and research ultrasound scanners, it was shown that the cortex can be imaged in vivo [7, 8]. These methods have only been applied on a limited number of individuals and the measurement of the cortical thickness, a key parameter for fracture risk assessment [9, 10], was only shown to be feasible in young healthy adult volunteers [7].

Bone loss occurring as part of the natural ageing process and accelerated in osteoporosis is associated with a degradation of cortical bone microstructure: unbalanced intracortical remodeling leaves cavities only partially filled with newly formed bone tissue and so-called giant pores due to the clustering of the remodeled cavities [11][12]. Porosity increases with age, e.g., in females from about 5% at 30 years old to 15% at 80 years old [13]. This is associated with an increase in pore diameter [14]. At the diaphysis of long bones, most of the cortical porosity is formed by so-called Haversian canals, which are roughly cylindrical and run nearly parallel to the bone axis. Previous studies have shown that the median pore diameter can vary from 40 to 200 µm between individuals, for cortical bone tissue with porosity ranging from 1 to 21% [15, 16, 11, 17].

Ultrasound echo signals reflected at the inner surface of the cortex (endosteum) are weak due to scattering by the microstructure and absorption in the viscoelastic mineralized collagen extracellular matrix [18, 19]. The amplitude of the echoes backscattered from the pores may be more important than that of echoes from the endosteal interface. As a consequence, a major challenge for bone ultrasound imaging is to image the endosteal interface despite strong attenuation

and diffuse scattering by the pores. In the degraded bones of osteoporotic subjects, characterized by a higher porosity and larger pores, stronger diffuse scattering by the pores is expected compared to healthy individuals. For instance, in ultrasound images from in-vivo measurements of an ongoing study, shown in Figure 1 for illustration, the endosteal interface is found to be more visible for a young volunteer (26 y.o) than for an older one (61 y.o). Because little research on bone ultrasound

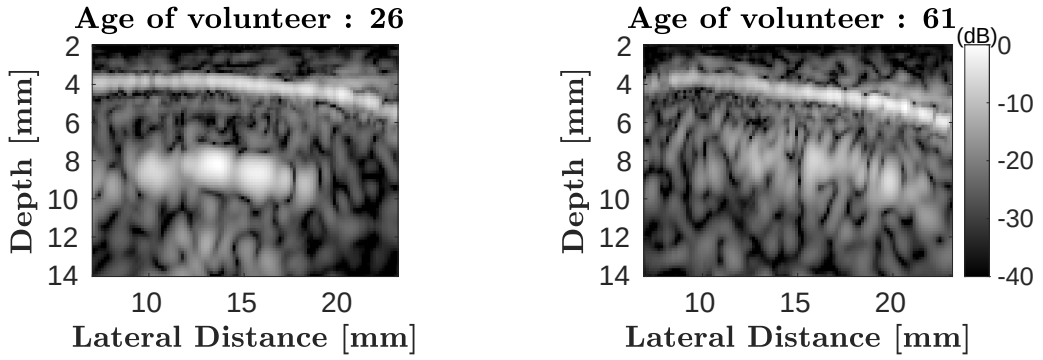

Figure 1: Illustration of degraded endosteal interface visibility with age on two subjects. Transverse ultrasound image of the tibia for two volunteers aged 26 (left) and 61 (right) are shown. The bright continuous line is the periosteal interface at a depth of about 4 mm which is perfectly visible for the two subjects. The endosteal interface at a depth of about 8 mm is more visible in the younger subject. Normalized gray scale dynamic range is given in dB. Images were obtained with a probe operating with a center ultrasound frequency of 2.5 MHz with a method similar to that described in [7].

imaging has been conducted until now, it is yet unknown to which extent it is possible to obtain an ultrasound image of the endosteal interface of human cortical bone, in particular in osteoporotic subjects.

The objective of this study was to quantify the influence of cortical bone microstructure on the identification of the endosteal interface in an ultrasound image in order to estimate the range of porosity and other microstructure variables, such as pore size, for which ultrasound imaging with a conventional beamformer would be feasible. Synthetic data from two-dimensional numerical simulations using a large set of real cortical microstructures with porosity ranging from 2% to 24% were generated. Images were reconstructed using a delay-and-sum algorithm with optimized f-number and correction of refraction at the bone-soft tissue interface. A similar algorithm was previously used in vivo and enabled to determine the cortical thickness of young healthy individuals [7].

2. Materials and Methods

2.1. Models of bone cortex and soft tissues

The two-dimensional (2D) models of bone cortex used for the simulations were generated using synchrotron X-ray microcomputed tomography (SR-μCT) three-dimensional images of human bone from a previous study [20]. Briefly, samples were collected in the mid-diaphysis of the femur of 29 subjects (16 females and 13 males, age range: 50-95 years old). The femurs were provided by the Département Universitaire d'Anatomie Rockefeller (Lyon, France) through the French program on voluntary corpse donation to science. The tissue donors or their legal guardians provided informed written consent to give their tissue for investigations, in accord with legal clauses stated in the French Code of Public Health. For each femur, two cuboids specimens of nominal size $3 \times 4 \times 5$ mm^3 were extracted, one in the lateral and the other in the medial quadrant. Three specimens which contained trabecularized cortex were discarded, resulting in a collection of 55 specimens for this study. SR-μCT images of the specimens were obtained with isotropic voxel size of 6.5 µm performed on the beamline ID19 at the European Synchrotron Radiation Facility (ESRF, Grenoble, France). The image processing was described previously in [21]. Briefly, the 3D volume of each specimen was cropped to a perfect rectangular parallelepiped shape and slightly rotated so that the geometric coordinates coincide with the material coordinates defined by the faces of the specimen. Thereafter, axis 3 was approximately along the direction of osteons (and diaphysis axis) and axes 1 and 2 were perpendicular to osteons. The images were then binarized by single level thresholding to obtain two phases: pores and mineralized matrix with an output voxel size of 10 µm, Figure 2.

For the 2D simulations, a set of 105 2D images were created by randomly picking slices in the (1,2) plane from the 3D image stack (Figure 2) of the 55 specimens. The 2D images were sorted so that their porosity (pore surface to total surface ratio) was ranging from 2% to 24%. For the critical range of porosity (7 -15) % in which strong variations of the image contrast are expected, we selected 5 times more slices than for low ($< 7\%$) and high ($> 15\%$) porosities.

Each 2D image of microstructure was used to build a model for numerical simulations: a three-layer medium representing the configuration used for imaging the diaphysis of a long bone with an ultrasound transducer oriented perpendicular to the bone diaphysis (Figure 3). Since the original microstructure images were too small (approximately 2.7×3.5 mm^2) to perform a realistic simulation, the bone layer was created by duplicating and mirroring the microstructure of

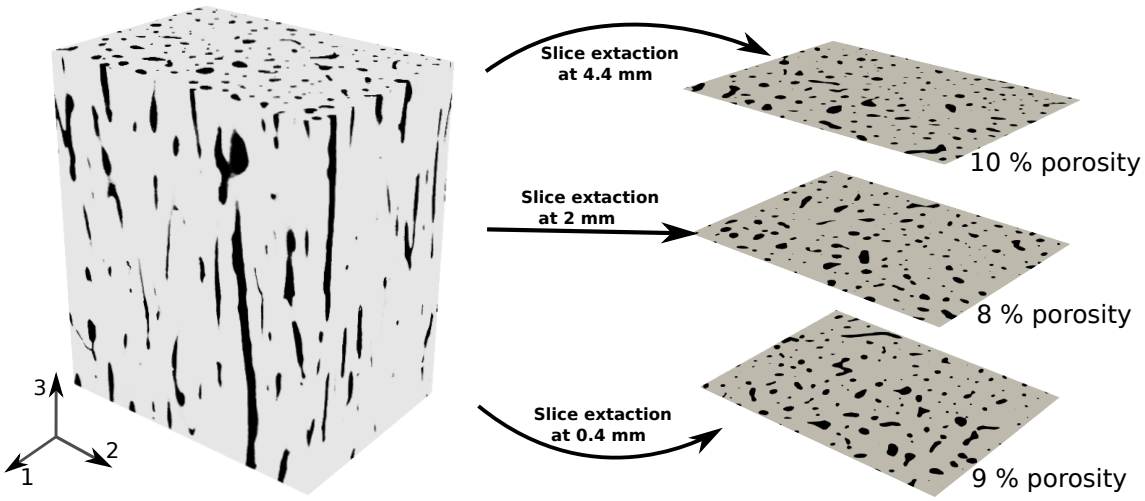

Figure 2: Binarized SR-μCT image of a cortical bone specimen of nominal dimensions $3 \times 4 \times 5$ mm^3 (original voxel size 6.5 µm). Black: vascular pores; light gray: mineralized matrix. Axis 1 corresponds to radial direction, axis 2 to the circumferential direction and axis 3 to the axial direction or diaphysis axis. For illustration, 3 slices extracted from the 3D volume, as used for 2D numerical simulations, are shown. 2D porosity values are given for each slice, illustrating the variable porosity in a 3D volume.

the original image in direction 2. A layer of soft tissue was placed above the cortical bone layer, to mimic the tissues between the probe and bone and a layer of marrow was placed below. The dimensions of the three-layer medium are given in Figure 3.

For the mineralized matrix of the cortical bone layer, the compressional and shear wave-speeds used in the simulation were 3496 m.s^{-1} and 1645 m.s^{-1} respectively. These values were deduced from the elastic coefficients of the bone matrix [21] (see Appendix A for details of the mass density and wave-speed estimation).

The material within the pores was assumed to be a fluid. The compressional wave-speed was 1610 m.s^{-1} for cutaneous tissue [22] and 1410 m.s^{-1} for marrow [23]. Ultrasound attenuation in cortical bone is due to a combination of absorption by dissipative mechanisms in particular in the mineralized matrix and scattering by the pores [24]. Following the models of Yousefian et al. [18, 25], a frequency-independent absorption within the bone matrix with an absorption coefficient of 19.0 dB/cm at 2.5 MHz was modeled.

2.2. Pores statistics

The microstructure for each model was characterized by cortical porosity (Ct.Por), cortical pore density (Ct.Po.Dn in pores/mm^2) and the distribution of pore diameters. These were calculated following the approach adopted by [26, 27]. Ct.Por was obtained by taking the ratio of the number

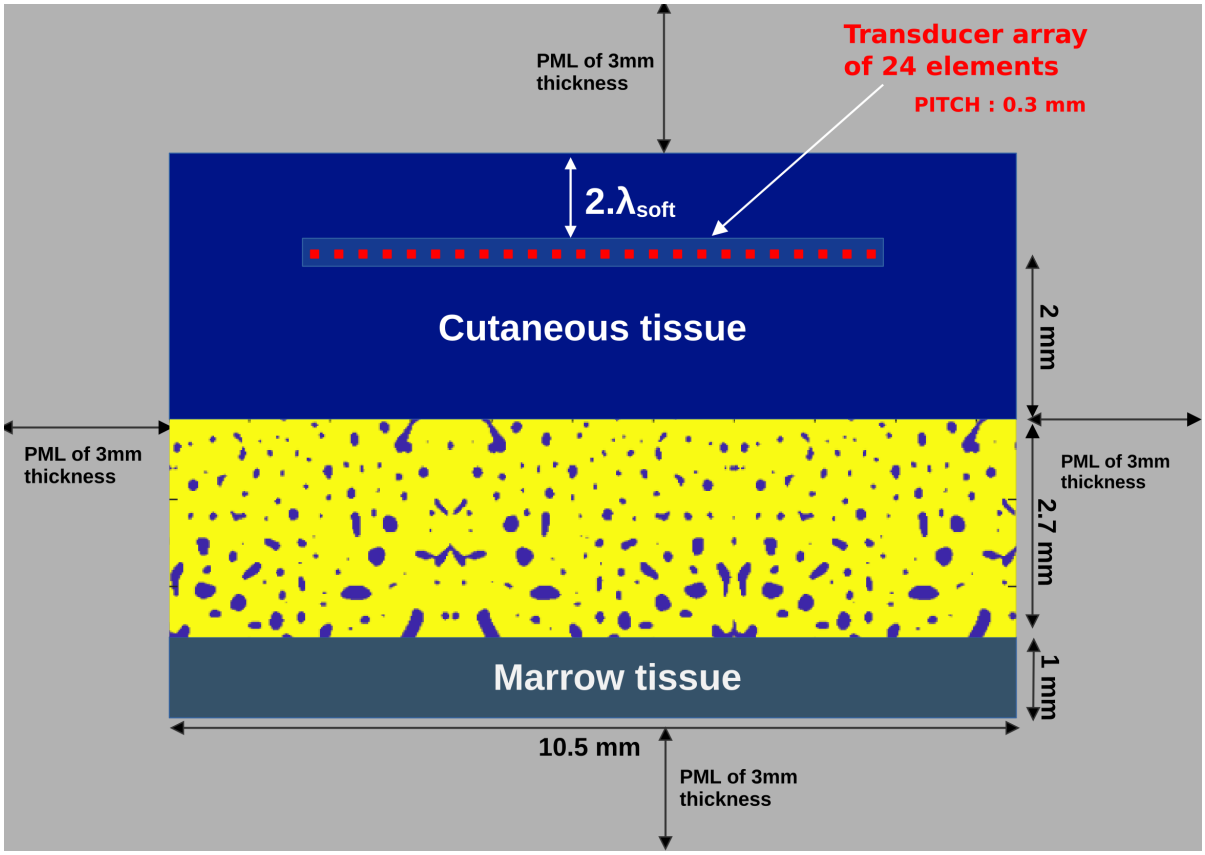

Figure 3: Three-layers model used for simulations: cutaneous tissue (blue), cortical bone tissue (yellow) and marrow tissue (bluish green) surrounded by Perfectly Matched Layers (PML, in gray).

of pixels associated with pores to the total number of pixels. Ct.Po.Dn was calculated as the number of pores divided by the total bone area. The diameter of each pore was calculated as the diameter of a disk of the same area. The distribution of pore diameters was characterized by the median value (Ct.Po.Dm); the 1^{st} (Dm.DC-1) and 9^{th} (Dm.DC-9) deciles; the average diameter of small pores (Sm.Po.Dm), i.e., of pore diameters smaller than Dm.DC-1; the average diameter of large pores (Lg.Po.Dm), i.e., of pore diameters larger than Dm.DC-9; the range of variation (Dm.Rng), i.e. the difference between the maximum and the minimum pore diameter; and the inter-decile range (Dm.IDRng).

In Figure 4 variations of Ct.Po.Dm and Ct.Po.Dn as a function of Ct.Por are plotted for the collection of microstructures used for the simulations.

2.3. Simulation of the ultrasound imaging sequence

We simulated the experimental configuration and acquisition sequence in [7] where an ultrasound array is placed on the skin to image the radius or tibia in a transverse plane, that is, in a

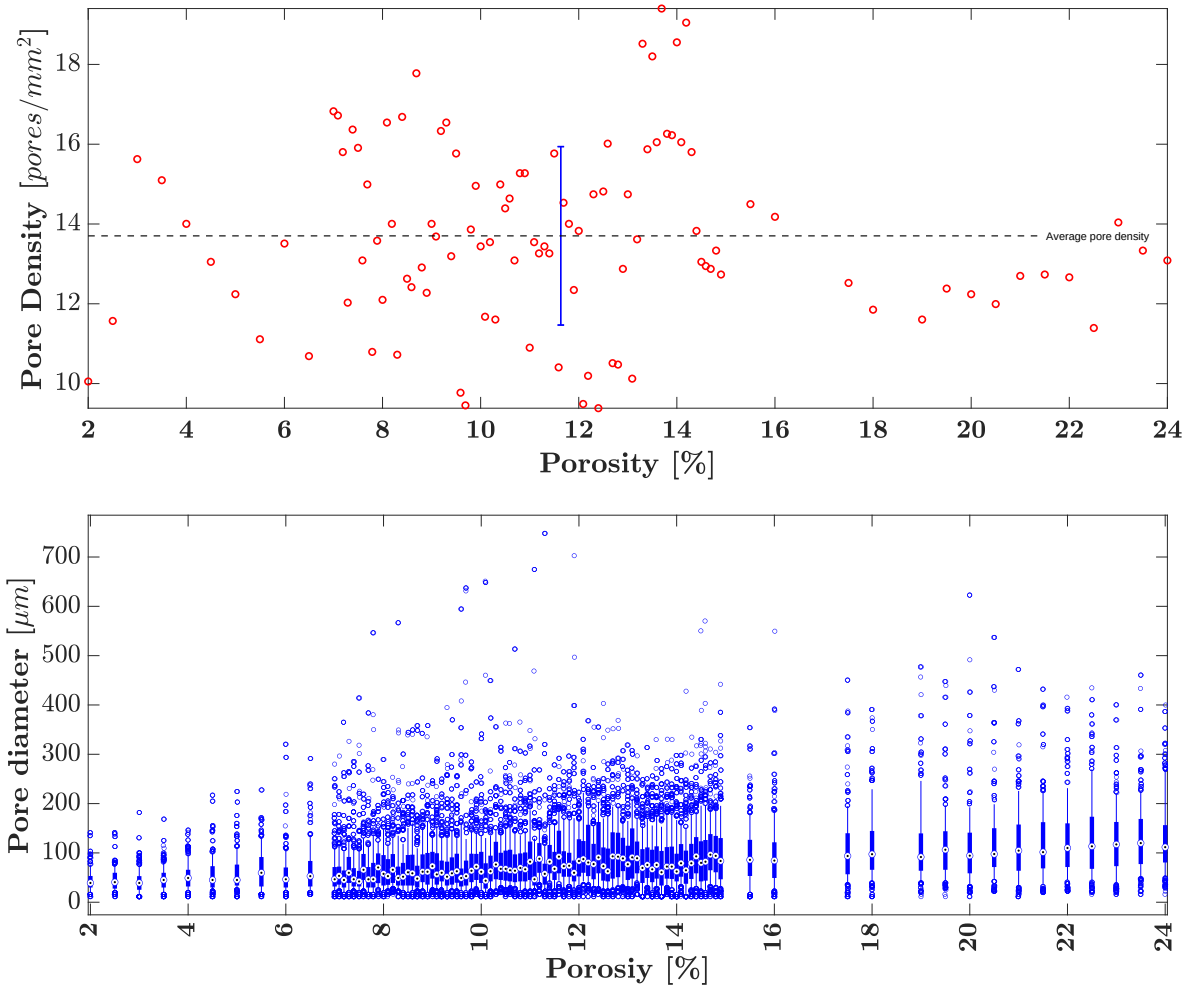

Figure 4: Pore statistics for each microstructure. Top: pore density (red circle) as a function of porosity; the black dashed line is the mean value and the standard deviation for the collection of microstructure is represented in blue. Bottom: stacked customized boxplots of pore diameter for each microstructure. Bottom and top of each box are respectively the first and last decile values, the circle in the middle of each box is the median pore diameter, the vertical line below each box extends from first decile to first quartile, the vertical line above each box extends from third quartile to ninth decile. Points below and above lines are respectively the values of diameters lower than the first decile and greater than the ninth decile

plane perpendicular to the diaphysis (and also perpendicular to the axis of the osteons). The simulated transducer mimicks the one used in the experiment except for the number of transducers. It is a 6.9 mm array with 24 elements and a pitch of 0.3 mm (element size of 10 µm, i.e. one grid step). The transducer is placed in the upper layer at a depth of 2 wavelengths to avoid border effects, and centered horizontally (Figure 3).

An acquisition scheme for synthetic aperture imaging was simulated: each individual element in the array successively transmitted a Gaussian-windowed tone burst with a central frequency of 2.5

MHz (3dB bandwidth= 1.33 MHz, see Figure 5). For each transmission, the backscattered signals were recorded by all the elements of the array. Therefore, for each bone microstructure, 24×24 backscattered synthetic signals were recorded.

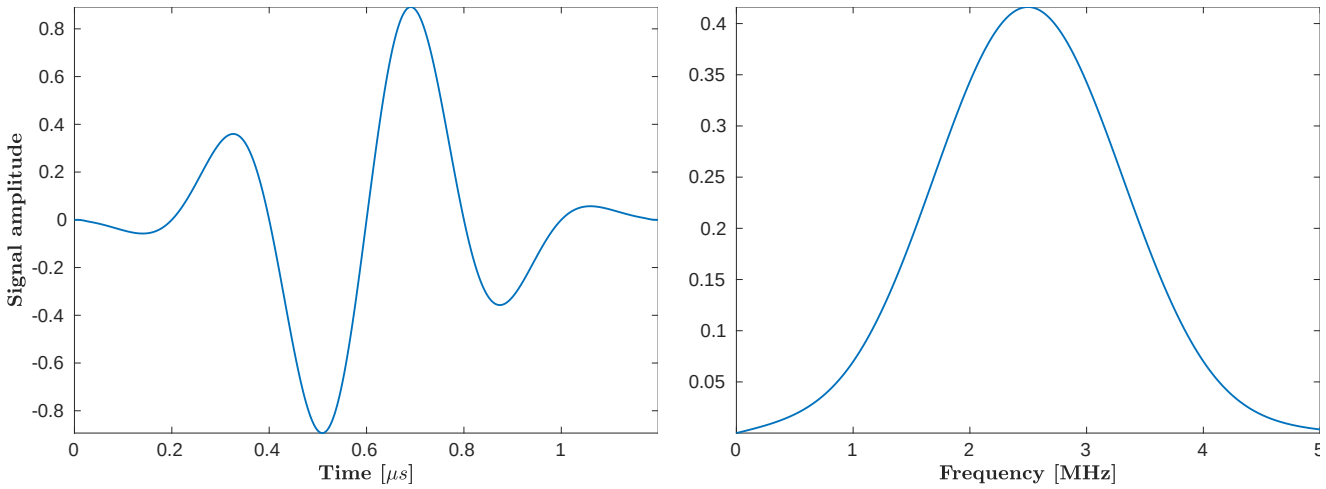

Figure 5: Emitted tone burst in temporal domain (left) and in frequency domain (right).

Elastic wave propagation in the three-layer medium was simulated with the Finite Difference Time-Domain (FDTD) open-source code SimSonic [28, 29]. To avoid reflections on the boundaries of the simulation domain, a Perfectly Matched Layer (PML) boundary condition (3 mm thickness, approximately 5 wavelengths in soft tissues) was set (Figure 3). The spatial grid size Δx for the FDTD simulation was equal to the microstructure image pixel size (10 µm). This leads to a mesh size equivalent to 56 points per wavelength in marrow at the center frequency, which is sufficient to model accurately the wave propagation with reasonably small numerical dispersion [30]. The simulation time step was chosen with respect to the Courant–Friedrichs–Lewy (CFL) stability conditions for 2D simulations. A constant value of $CFL = 0.99$ was used for these simulations.

2.4. Cortical bone wave-speed estimation

The ultrasound wave-speed in the bone layer (Figure 3) must be known to perform the refraction corrected image reconstruction as proposed in [7]. It is a priori unknown as it depends on the specific microstructure considered. Note that the combination of the isotropic elastic properties for the bone matrix with the quasi-random distribution of the pores in the plane $(1, 2)$, leads to isotropic properties in this plane at the scale of the wavelength, which is also the millimeter scale or mesoscale [31]. Additional simulations were performed in order to estimate this wave-speed. A plane wave at normal incidence was emitted by the array using the signal shown in Figure 5.

Virtual receivers were placed inside bone along 5 equally spaced lines (spacing=0.5 mm) parallel to periosteal and endosteal interfaces. The waveforms recorded on each line of receivers were coherently summed and the time-of-flight was estimated from the first received signal peak. The wave-speed in the cortical bone is finally obtained by linear regression of time-of-flights measured at the 5 different depths (see Figure B.13 in Appendix B). As an alternative method, the wave-speed could be obtained by finding within a range of values, the wave-speed that maximizes the focus quality at the endosteal interface as it was done in in-vivo [7].

2.5. Image reconstruction with a refraction-corrected delay-and-sum algorithm

Delay-and-sum (DAS) algorithm with a constant f-number in receive throughout the image is used for image reconstruction [32]. DAS was chosen as it is the most extensively used beamforming algorithm, and also because it was used for the first in-vivo imaging of the bone cortex in [7]. A hanning window was applied to the receiver sub-aperture. A preliminary study aimed to determine the optimal f-number that maximizes the image contrast for the detection of the endosteal interface, the optimal f-number was 1.9 (see Appendix C). This way, DAS is used at its highest potentiality as described by [32]. The synthetic aperture sequence led to 24 low resolution images which were coherently summed to get a high contrast image. The delays used in the DAS algorithm account for refraction at all the interfaces. The implementation described in [7] was used to calculate the delays: for each array element and image pixel, Fermat's principle is used to calculate the travel time through the multi-layered medium. Only the contribution of longitudinal waves were considered, i.e. the arrival times of wave contributions associated with the shear waves were disregarded. The ultrasound longitudinal wave-speed used for the bone layer was different for each microstructure as explained in section 2.4.

2.6. Endosteal interface visibility quantification

To evaluate image quality, i.e., the visibility of interfaces, the relative interface contrast (C_{EP}) and the endosteal interface contrast (C_{EI}) were defined as follows:

$$C_{EP} = \frac{\mu_E}{\mu_P} \quad ; \quad C_{EI} = \frac{\mu_E}{\mu_I},$$

where μ_I, μ_E and μ_P are respectively the average image intensities in the center of the cortex, at the endosteal and periosteal interfaces. The regions of interest (ROI) used for the calculation of μ_I, μ_E and μ_P, are defined in Figure 6 where the red box represents the inner bone ROI, the yellow

and blue boxes represent respectively the periosteal interface ROI and the endosteal interface ROI. Each ROI had a height of 0.8 mm and a width of 6.5 mm.

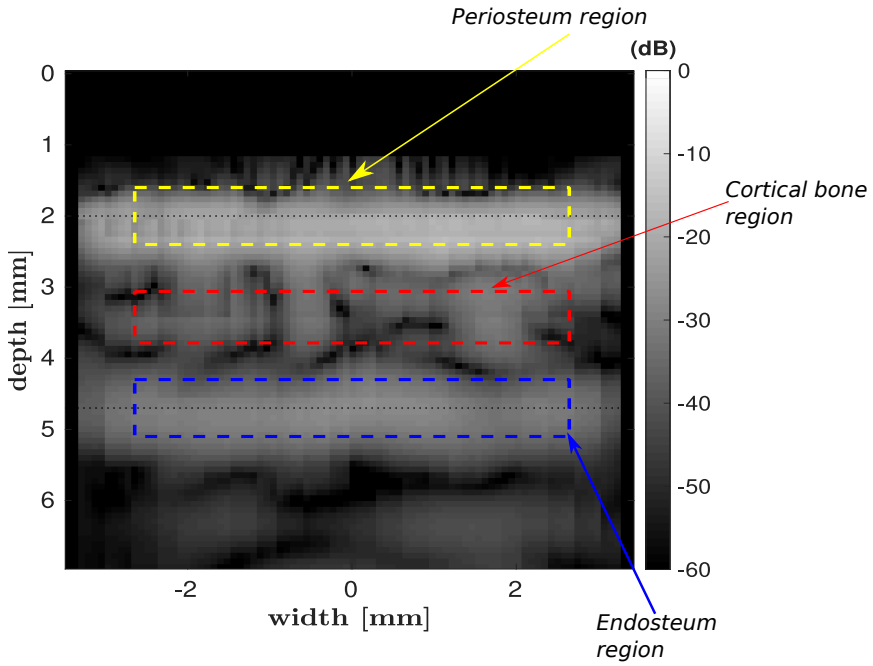

Figure 6: A typical reconstructed image for the simulation configuration shown in Figure 3. The yellow, red and blue ROIs were used to evaluate periosteum, inner bone, and endosteum contrasts, respectively.

Because the amplitude of the reflection at the periosteal interface is only slightly influenced by the porosity, C_{EP} variations reflect the variations of the absolute visibility of the endosteal interface. C_{EI} evaluates how well the endosteal interface can be distinguished from the speckle inside the bone. On decibel scale, a positive value of C_{EI} means that endosteal interface is clearly visible while a negative value means that the endosteal interface is poorly visible.

2.7. Data Analysis

A correlation analysis was conducted to identify the microstructure parameters defined in 2.2 of most important influence on endosteal interface visibility metrics (C_{EI} and C_{EP}). Normality of the distribution of the variables was evaluated using the Shapiro-Wilk test and we found that most of the variables were not normally distributed. Therefore, Spearman rank coefficients were used.

Correlations were considered statistically significant for $p < 0.05$. Statistical analyses were made using the Matlab 2018b Statistics Toolbox (Mathworks Inc., Natick, MA, USA). The pat-

terns of variation of C_{EI} and C_{EP} with the three most important microstructure parameters were investigated. The purpose was to assess the range of values of the microstructure parameters, in particular porosity, for which the endosteal interface is visible.

Finally, the collection of images from all microstructure are analyzed and characteristic images to best illustrate the effect of the microstructure parameters on the appearance of the endosteal surface in the images were selected.

3. Results

3.1. Wave-speed in cortical bone models

Figure 7 shows the wave-speed in cortical bone estimated for each microstructure as a function of Ct.Por . Wave-speed varied from about 2900 to 3400 m.s^{-1} as cortical porosity decreased from 24 to 2 %, that is a variation of wave-speed of about 16%.

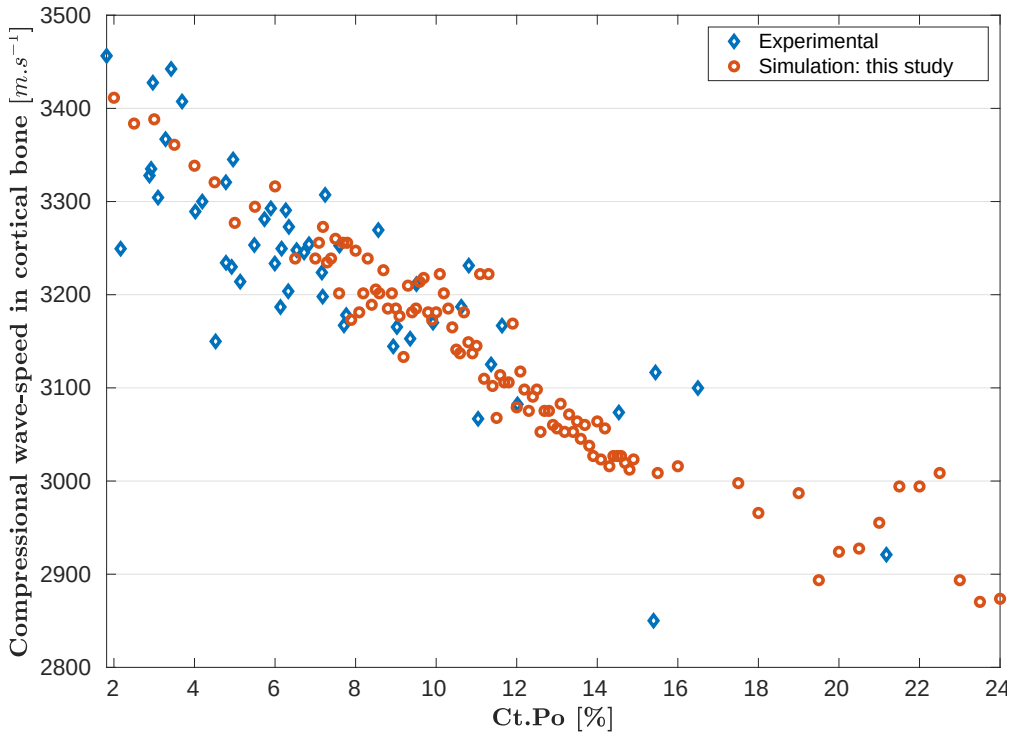

Figure 7: Simulated (red circles) and experimental (blue diamonds) wave-speed against porosity (Ct.Por).

For comparison, experimental values that were deduced from experimental elastic coefficients obtained by Cai et al. [33] on the same collection of bone specimens (see in Appendix B the details on experimental wave-speed determination) are also shown. Linear regression models between wave-speed and Ct.Por for both experimental ($V_1^{exp} = 3404.5 - 23.83 \times Ct.Por$, $RMSE =$

61.9 m.s^{-1}) and synthetic data ($V_1^{sim} = 3406.5 - 23.73 \times Ct.Por$, $RMSE = 37.8$ m.s^{-1}) had very close parameters and were in accordance with literature [34].

3.2. Descriptive statistics

The values of microstructural properties, wave-speed in cortical bone and interface visibility metrics are summarized in Table 1

	Median	QT-1	QT-3	MIN	MAX
Ct.Por [µm]	11.19	8.57	13.83	2.00	24.00
Ct.Po.Dm. [µm]	67.70	57.26	84.81	39.09	119.95
Ct.Po.Dn. [pores/mm^2]	13.51	12.27	15.27	9.38	19.40
Dm.DC-1 [µm]	25.23	22.57	31.92	15.96	52.93
Dm.DC-9 [µm]	155.98	133.51	186.05	73.99	271.05
Lg.Po.Dm [µm]	213.01	186.06	238.79	97.95	337.39
Sm.Po.Dm [µm]	18.20	15.27	22.53	11.28	38.42
Dm.Rng [µm]	323.45	273.90	392.15	129.65	736.69
Dm.IDRng [µm]	132.62	106.56	154.74	54.04	229.13
V_1^{sim} [m.s^{-1}]	3137.13	3050.90	3210.75	2870.30	3411.42
C_{EI} [dB]	0.86	−0.59	3.33	−8.31	18.57
C_{EP} [dB]	−6.81	−8.15	−5.20	−11.35	−1.89

Table 1: The median, minimum value (MIN), maximum value (MAX), first (QT-1) and last (QT-3) quartile of the visibility metrics (C_{EI}, C_{EP}), the wave-speed in cortical bone and the pore microstructural variables (defined in section 2.2)

3.3. Influence of microstructure on image contrasts

Spearman rank correlation coefficients between image quality metrics (C_{EI}, C_{EP}) and pore characteristics are given in Table 2. Ct.Po.Dn was not significantly correlated to the interface metrics, therefore it was discarded for the rest of the analysis. Negative correlations were found for the rest of the variables. Among all variables, the strongest correlation coefficients were for Lg.Po.Dm, Ct.Por, Dm.IDRng, and Dm.DC-9 (r_s from -0.61 to -0.71, $p < 0.001$). Correlation for Dm.Rng and Ct.Po.Dm were moderate (r_s from -0.48 to -0.52, $p < 0.001$). Smaller correlations for Dm.DC-1 and Sm.Po.Dm (r_s from -0.23 to -0.33, $0.001 < p < 0.05$) were found.

Pore characteristics	C_{EI}	C_{EP}
Lg.Po.Dm	-0.71^{2}	-0.67^{2}
Ct.Por	-0.66^{2}	-0.63^{2}
Dm.IDRng	-0.65^{2}	-0.61^{2}
Dm.DC-9	-0.62^{2}	-0.59^{2}
Dm.Rng	-0.52^{2}	-0.48^{2}
Ct.Po.Dm	-0.50^{2}	-0.48^{2}
Dm.DC-1	-0.33^{1}	-0.29^{1}
Sm.Po.Dm	-0.27^{1}	-0.23^{1}
Ct.Po.Dn	$0.08^{n.s}$	$0.11^{n.s}$

Table 2: Spearman correlation coefficient r_s between image quality metrics and microstructural properties. C_{EI}: endosteal-interface contrast, C_{EP}: relative interface contrast . $^{n.s}$: not significant $p > 0.05$, ^{1} : $0.001 < p < 0.05$, ^{2} : $p < 0.001$

In figure 8, the variations of averaged pixel intensity in the three ROIs, C_{EI} and C_{EP} are shown for all microstructures as function of Lg.Po.Dm, Ct.Por, and Dm.IDRng which were found to be the most important variables (Table 2). Each point corresponds to a specific microstructure. First, we observe the relatively small variations of the periosteum mean intensity (blue curve) with respect to microstructure parameters. As a consequence, C_{EP} essentially evaluates endosteal interface contrast. As expected, this value is always negative because the endosteal surface is less visible than the periosteal surface.

Second, endosteal interface mean intensity (red curve) decreases while that of the internal bone speckle intensity (orange curve) increases for increasing values of microstructure parameters reflecting the degradation of bone microstructure. C_{EI}, which is by construction our metric best reflecting the visibility of the interface, varies between about -5 dB and 15 dB. Negative values correspond to speckle intensity inside bone larger than endosteal interface intensity. For small "large pore" size (Lg.Po.Dm $<$ 200 µm), low cortical porosity (Ct.Por $<$10%) and weak pore size dispersion (Dm.IDRng $<$ 100 µm), C_{EI} is positive for most of the microstructures while it is negative for large "large pore" size (Lg.Po.Dm $>$ 250 µm), high cortical porosity (Ct.Por $>$ 15%) and strong pore size dispersion (Dm.IDRng $>$ 170 µm). For intermediate values, C_{EI} hovers around 0 dB.

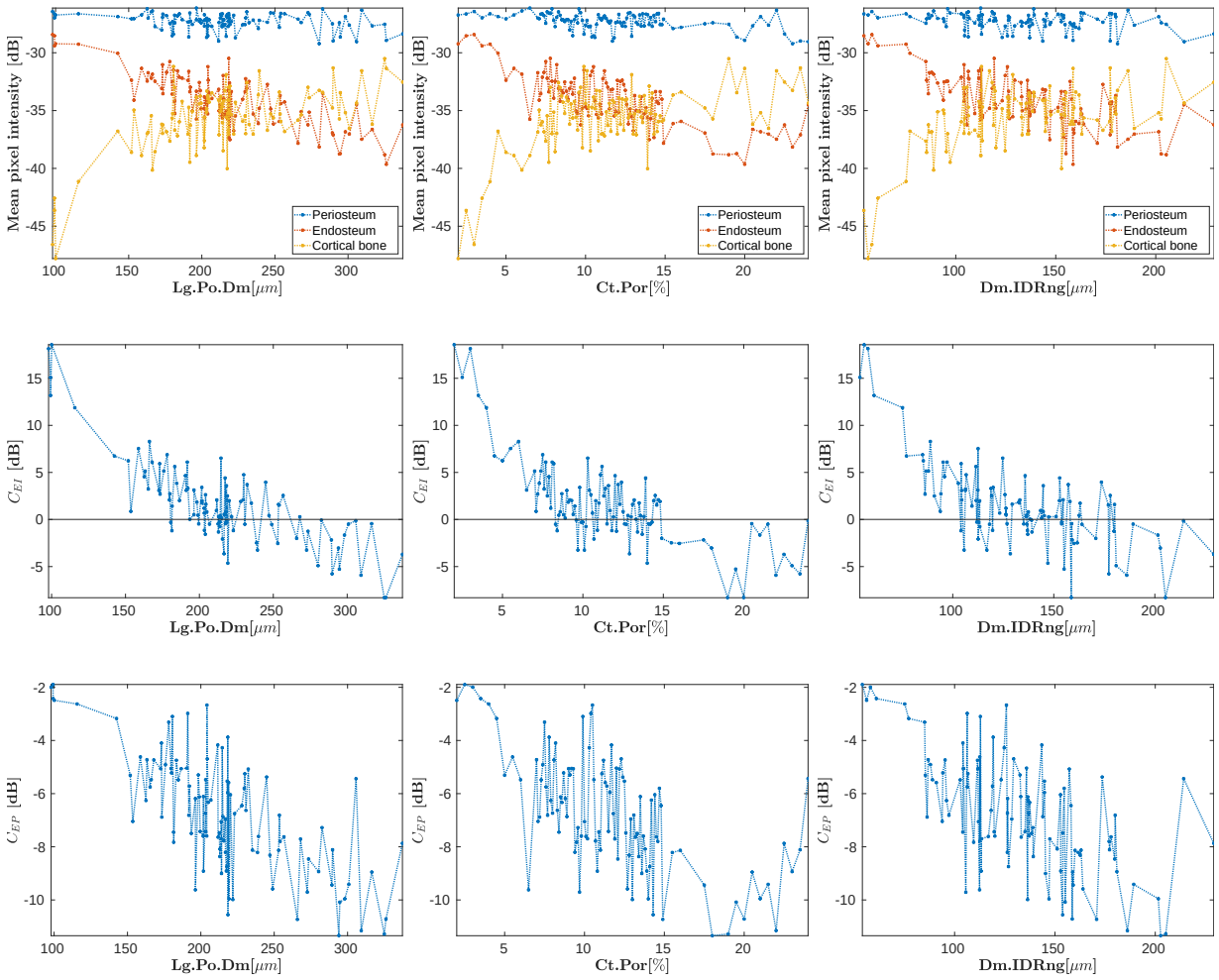

Figure 8: Average pixel intensity for the three ROIs (top), bone-endosteum contrast C_{EI} (middle) and interface contrast C_{EP} (bottom). The evolution of these variables for "large pores" size (Lg.Po.Dm), porosity (Ct.Por), and pore diameter dispersion (Dm.IDRng) are shown.

The reconstructed images for all microstructures are provided in the supplementary material. In the following, a set of representative images are presented. Figure 9 shows a selection of images for different porosity values. Lg.Po.Dm and C_{EI} are given for each image. The periosteal interface is clearly visible as a bright zone centered at 2 mm-depth. The endosteal interface at 4.7 mm-depth is more or less visible depending on the microstructure. With increasing porosity, speckle intensity inside bone increases and endosteal interface visibility fades. On these images, for porosities of 2, 5, and 8% the endosteal interface stands out from inner cortical bone speckle and C_{EI} values are positive. For porosities of 13, 16 and 20 %, speckle intensity inside the bone becomes dominant, the endosteal interface can hardly be distinguished, and C_{EI} values are negative.

As Lg.Po.Dm was found to be relatively strongly correlated to the image contrast, Figure 10

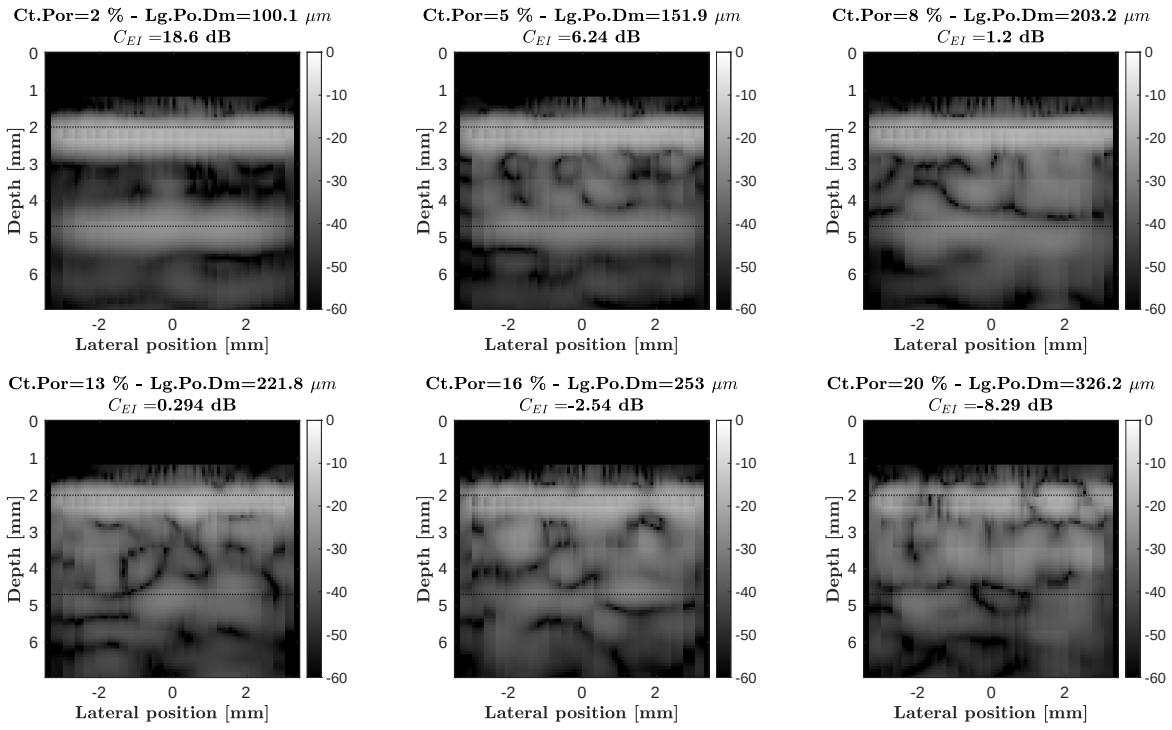

Figure 9: Reconstructed ultrasound images from simulated data for six microstructures for increasing porosties. 1^{st} row (from left to right): 2, 5 and 8 % porosity, 2^{nd} row: 13, 16 and 20% porosity. Lg.Po.Dm and C_{EI} are given for each image. The black dotted lines represent the true positions of the periosteal and endosteal interfaces. Each image is reconstructed using DAS with an optimized receive f-number of 1.9. The intensity is log-compressed and displayed with a dynamic range of 60 dB.

shows reconstructed images for microstructures with a similar porosity around 10.5% (±1%), and with increasing Lg.Po.Dm spanning the range $183-272$ µm. For these microstructures, C_{EI} values decreased from 5.63 dB to -3.25 dB. Endosteal interface is visible for images on the first row whilst it is not for the images on the second row. As an example, figure 10 shows that the endosteal interface is perfectly detectable ($C_{EI} = 5.63$ dB) for 11.19 % porosity and Lg.Po.Dm= 183.3 µm and not visible ($C_{EI} = -3.25$ dB) for 10.09 % porosity and Lg.Po.Dm= 239.3 µm, illustrating a strong influence of the diameter of large pores on the image contrasts.

4. Discussion

4.1. Impact of the intra-cortical microstructure on image contrast

In this study, the effect of cortical bone microstructure on the quality of ultrasound images of the cortex is investigated. The contrast should be sufficient to allow the identification of the endosteal interface in order to assess cortical thickness, an important biomarker of bone health

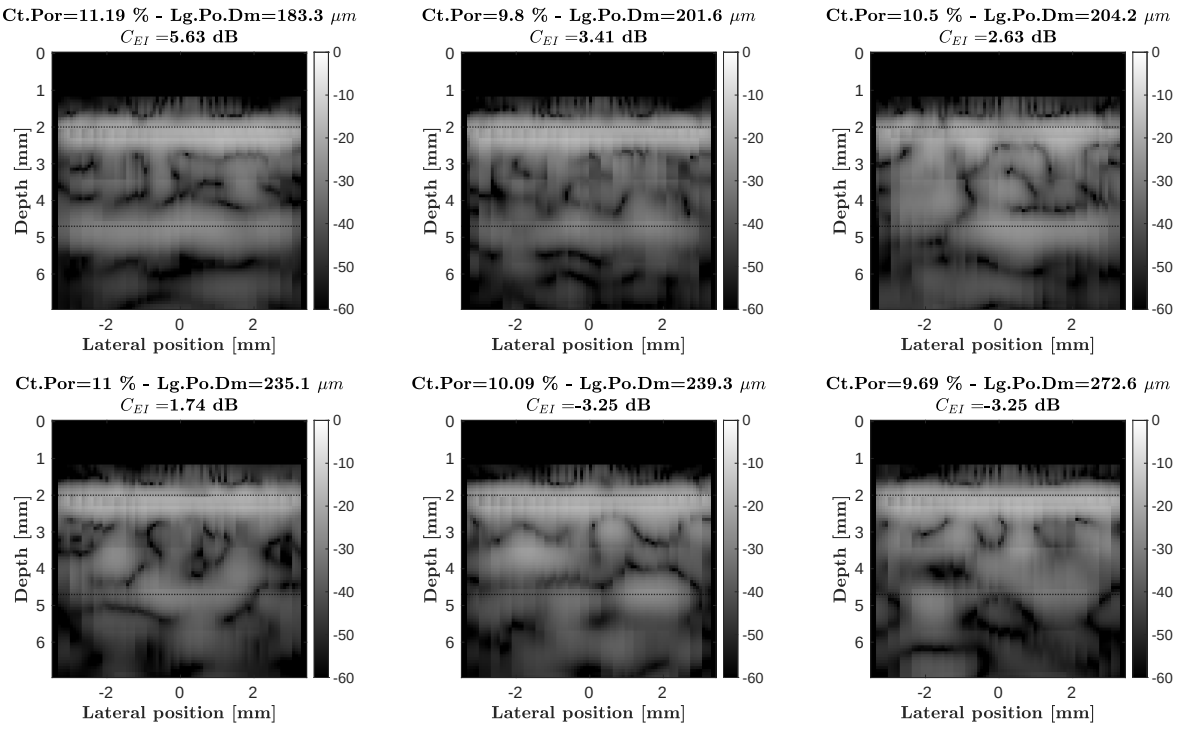

Figure 10: Reconstructed ultrasound images from simulated data for six microstructures with nearly equal porosity (around 10.5%) but increasing "large pore" size (Lg.Po.Dm). Ct.Por and C_{EI} are given for each image. The black dotted lines represent the true positions of the periosteal and endosteal interfaces. Each image is reconstructed using DAS with an optimized receive f-number of 1.9. The intensity is log-compressed and displayed with a dynamic range of 60 dB.

[5, 35]. Numerical simulations with a collection of 105 high-resolution images of microstructure (porosity ranging from 2 to 24%) were used in order to cover the diversity of porosity, pore size and pore distribution met in human cortical bone. Indeed, with ageing and osteoporosis, cortical bone porosity and pore size increases. This degradation of the microstructure is challenging for ultrasound imaging.

The simulation framework was validated based on the excellent agreement found between experimental wave-speed values and those recovered from numerical simulations (Figure 7 and Appendix B). Image reconstruction was performed using the state-of-the-art delay-and-sum image reconstruction with optimized receive f-number, correction of refraction at the soft tissue-bone interface and sample-specific wavespeed. A signal processing approach similar to the one adopted by [7] for in vivo imaging of the cortex of young adults were employed.

It is found that as Ct.Por increases, speckle intensity inside the bone cortex increases whereas the intensity of the signal from the endosteal interface decreases (Figure 8 and Figure 9). We found

a reduction of approximately 18 dB in endosteal visibility metric (C_{EI}) from the denser bones to the most degraded microstructures. Interestingly, the presence of large pores (quantified by Lg.Po.Dm and Dm.DC-9) and the width of the distribution of pore size (Dm.IDRng) had a strong effect on image contrast (see Table 2). For similar porosities, a microstructure with larger "large pores" will be associated to lower visibility of the endosteal interface (Figure 10). This means that the sole augmentation of cortical porosity is not enough to explain the contrast deterioration (see figure 11 for illustration). Overall, the endosteal interface was visible ($C_{EI} > 0$ dB) for microstructures with

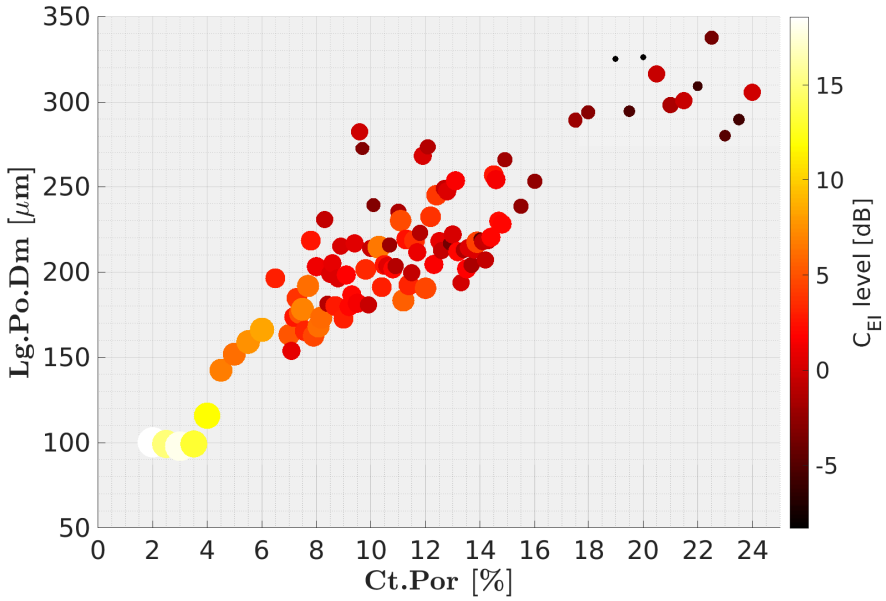

Figure 11: Scatter plot of endosteal interface contrast (C_{EI}) as a function of cortical porosity (Ct.Por) and diameter of large pore (Lg.Po.Dm). Size and color of each circle are proportional to the value of C_{EI}

moderate porosity (Ct.Por$\sim<$ 10%), small "large pore" size (Lg.Po.Dm $<$ 200 µm), and weak pore size dispersion (Dm.IDRng $<$ 100 µm). Endosteal interface was not visible ($C_{EI} < 0$ dB) for big "large pore" size (Lg.Po.Dm $>$ 250 µm), high cortical porosity (Ct.Por $>$ 15%) and wide pore size dispersion (Dm.IDRng $>$ 170 µm). These threshold values of the microstructure parameters are specific to our study as they are tied to the chosen central ultrasound frequency (2.5 MHz) used in vivo and cortical thickness (2.7 mm). For higher frequencies, ultrasound waves would experience stronger scattering by pores and higher attenuation resulting in lower threshold Ct.Por and Lg.Po.Dm values for a visible endosteum at the same depth.

4.2. Possible physical origins of contrast loss

The failure to observe the endosteal interface for degraded microstructures may be explained by several factors. The amplitude of the waves reflected at the endosteal interface decreases with increasing porosity because the effective acoustic impedance mismatch between bone and marrow is reduced. This can be quantified from the theoretical reflection coefficient (calculated for the acoustic power) which drops by 25% (corresponding to −1.2 dB in an image, see Appendix D) in the porosity range investigated. Therefore, the variations in the reflection coefficient cannot explain the 8 dB decrease in the intensity of the endosteal interface (Figure 8). Another factor is the attenuation that varies from about 20 dB/cm to 60 dB/cm in the investigated porosity range (see Appendix E). This corresponds to a decrease in the amplitude of backscattered echoes of about 20 dB if a round trip distance through the thickness of the cortex is considered. This value is larger than the observed 8 dB reduction of the amplitude at the endosteal interface. Because the proposed contrast metrics are calculated in the 0.8 mm-high regions of interest depicted in Figure 6, it is likely that our approach cannot accurately track further decrease in the amplitude of the specular reflection at the endosteal interface as the porosity increases. Indeed, because half the region of interest of the endosteal interface encompasses cortical bone, the amplitude at the endosteal interface shown in Figure 8 contains both specular reflection at the endosteal interface and diffuse scattering by the pores near the endosteal interface. The main reason for the loss of endosteal contrast could be the increase in the scattering strength from the inner microstructure of the cortex as porosity increases. For a porosity larger than 15 %, the amplitude of echo signals generated by the inner microstructure overcomes the amplitude of echo signals reflected at the endosteal interface. As a consequence, the endosteal interface is no longer visible. As shown in Figure 8, the speckle amplitude inside the cortex increases by about 10 dB (excluding extreme values) as the porosity increases. The product ka where k is the wavenumber at central frequency and for a wave speed of 3200 m/s, and a is the radius of the pores in the range 25 to 300 µm, varies from 0.12 to 1.5. Based on simulations similar to those of this study (but with monodisperse circular pores), Iori et al [36] found an increase of the backscatter intensity of about 5 dB as ka increased from 0.1 to 1, for ka between 1 and 1.5 a small decrease of about 2 dB was observed. This increase of pore backscatter intensity with ka supports the idea that the presence of large pores is the main cause of the loss of contrast at the endosteal interface.

4.3. Design of the numerical study: motivations and advantages

Our aim was to quantitatively assess the relationships between the bone microstructure and image contrast. This study was conducted with numerical simulation for several reasons. Firstly, this allowed us to investigate a large range of realistic microstructure types. This would not be possible in an in vivo study due to the limitations in X-ray imaging resolution in vivo, nor in an ex vivo study for which the number of samples and the control of their variability is an issue. One strength of the present study is to use high resolution images of human cortical bone obtained with SR-μCT, which reveal the realistic details of the microstructure of human cortical bone. Second, simulations of the imaging process are free of electronic noise and other experimental artifacts, resulting in a best-case imaging scenario. Finally, a plate-like cortical thickness with parallel interfaces was designed as the simplest imaging configuration to isolate the effect of varying microstructure from those of varying thickness and interface curvature or interface tilt. Interface curvature and tilt can be accounted for with the refraction corrected image reconstruction algorithm used here [7].

4.4. Limitations of the study

The original microstructure images obtained with SR-μCT were relatively small (2.7×3.5 mm^2). Other high resolution imaging modalities could have been used to generate the model, such as scanning acoustic microscopy [37]. The advantage of using SR-μCT images was the high resolution (voxel size of 6.5 µm) and high contrast providing an accurate picture of the pores. Although the vast majority of simulations of ultrasound propagation in cortical bone has been conducted in 2D configurations in the plane transverse to osteons [8, 26], the validity of this configuration has not been investigated in detail. Haversian canals are not infinite cylinders as hypothesized here but their average length is in the range of 2-4 mm [38]. Volkmann canals, which run nearly perpendicular to Haversian canals, contribute to a part of the porosity and are not modeled in 2D configurations. Another three-dimensional feature not considered here is the spatial resolution in the elevation dimension of the probe which is finite and results in a summation of the backscattered signals over the height of the elements of the probe array. In cortical bone, attenuation due to pore scattering and absorption within the bone solid matrix both contribute to the total attenuation coefficient. In these simulations, a frequency-independent absorption within the bone matrix is modeled with an absorption coefficient of 19.0 dB/cm at 2.5 MHz following Yousefian et al. [18], [25]. This value leads to a total attenuation slightly higher than the values reported by Grimal

et al [39] from ex-vivo measurements of attenuation in human cortical bone specimens. They reported an attenuation of about 50 dB/cm at 4 MHz for specimens with a porosity around 10% while in the present simulation study we found an attenuation of 40 dB/cm at 2.5 MHz for the same porosity (see Appendix E). Some simulations were also conducted without absorption within the bone matrix (results not shown) and the results were found to be similar. Accordingly, we believe that the conclusions of this study are not sensitive to the choice of the absorption coefficient in the matrix. Finally, the heterogeneity of the distribution pore sizes was not fully considered. Specifically, a gradient of pore sizes through the cortex was only present in a few microstructure images, and the roughness of the endosteal interface due to the presence of large pores across the interface (trabecularization) [40] was not considered. The impact on image quality of this heterogeneity should be investigated in a separate study.

4.5. Conclusion and perspectives

The simulation results presented in this article suggest that the cortical thickness of individuals with low and moderate porosity can be successfully imaged at 2.5 MHz. This is in line with the in vivo results of Renaud et al. [7] on two young subjects for which the endosteal interface could be clearly identified at the radius and tibia. In contrast, our results suggest that imaging the cortical bone of some elderly subjects or osteoporotic subjects with a degraded microstructure (porosity larger than 10%, presence of large pores) [14] would be challenging. Specifically, we have found that the presence of large pores is detrimental to image quality. Such large pores are characteristic of degraded bone and were associated with weak femoral strength ex vivo [35] and with fracture risk [41]. This may appear to be a major obstacle to bone imaging for some individuals with a high risk of fracture. A central frequency of 2.5 MHz like in in vivo measurements [7] is used. With a lower frequency, scattering and absorption may be reduced, however the spatial resolution in the ultrasound image may be not sufficient to clearly distinguish the endosteal interface from the periosteal and measure the cortical thickness. In this study we have used an optimally-implemented delay-and-sum image reconstruction algorithm, and demonstrated the limits of this approach. Advanced signal processing and image reconstruction could be considered to overcome this limitation, including data adaptive beamforming, specular beamforming, inverse problem and machine learning approaches [42, 43, 44, 45].

Appendix A Estimating the bone matrix characteristics

The material properties of the bone matrix tissue used for the numerical simulations of the propagation of elastic waves were derived from experimental data as described below.

Mass density. The bone matrix mass density (ρ^m) was deduced from measurements of the apparent mass density (ρ) and cortical porosity (Ct.Por) of 55 cortical bone specimens from elderly donors [33] (the microstructures used in the present study came from the same samples). A linear regression between ρ and Ct.Por is determined:

$$\rho = \rho^m - 13.1 \times \text{Ct.Por}$$

where ρ^m is the intercept for a null porosity. The correlation between ρ and Ct.Por was strong: Adj-R^2 = 84.5 %, p= 2.43 10^{-23}, RMSE = 22.1 kg.m^{-3}. Finally, a value of 1996 kg.m^{-3} was found for ρ^m. Figure A.12 shows the values of ρ as a function of cortical porosity along with the linear fit.

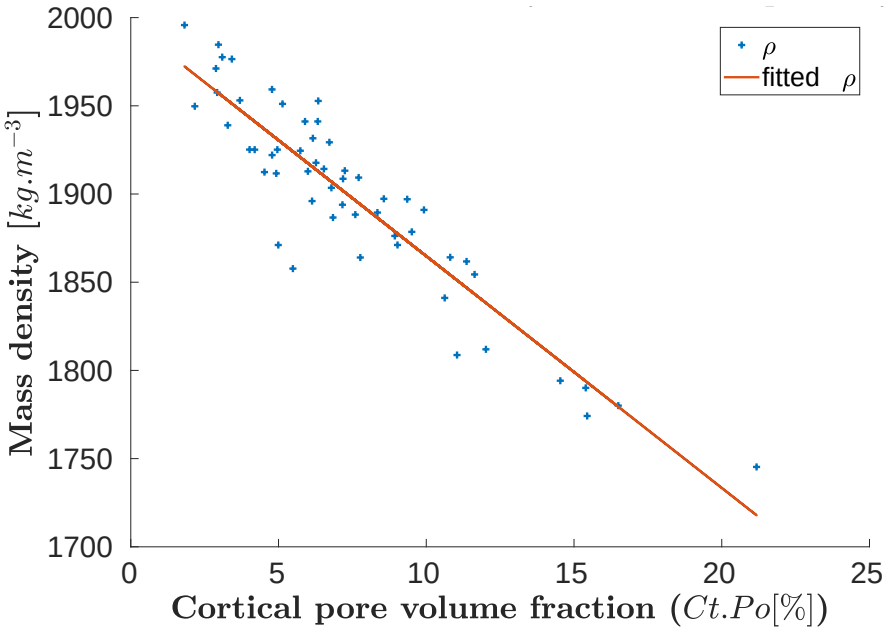

Figure A.12: Cortical bone apparent mass density (ρ) of the 55 human bone specimens of this study obtained by [33]. A regression linear model is fitted (red line).

Shear and compressional wave-speeds. Longitudinal and shear wave speeds in the bone matrix are deduced from ρ^m and experimental values of the matrix elastic coefficients C^m_{ij} (using Voigt notation, with $i, j = 1, 2, 3$) provided by Cai et al.[33] for the same bone specimens. For this study,

V_1^m and V_{12}^m were used, they are respectively the velocities of longitudinal and compressional waves propagating in bone matrix in the plane perpendicular to the bone axis and with in-plane particle motion. They are determined using:

$$V_1^m = \sqrt{\frac{C_{11}^m}{\rho^m}}, \quad and \quad V_{12}^m = \sqrt{\frac{C_{66}^m}{\rho^m}}.$$

Cai et al. [33] reported $C_{11}^m = 24.5$ GPa and $C_{66}^m = 5.4$ GPa, from which values of 3496 m.s^{-1} and 1645 m.s^{-1} were deduced for V_1^m and V_{12}^m respectively.

Appendix B Experimental ultrasonic velocity estimation for different cortical porosities

Cai et al [20] measured the stiffness tensor (C_{ij}), apparent mass density (ρ), and vascular porosity of cortical bone specimens from elderly donors. The compressional wave-speed for each specimen was calculated as $\sqrt{\frac{C_{11}}{\rho}}$, where C_{11} is the specimen-specific elastic coefficient corresponding to longitudinal deformation in the plane of isotropy. The obtained values of wave-speed in direction 1 (any direction normal to the symmetry axis of the microstructure) as a function of the intra-cortical porosity are shown in Figure 7 in blue diamonds. The red circles in Figure 7 represent the values of wave-speed estimated from this study using the method described in section 2.4 and the configuration of Figure B.13.

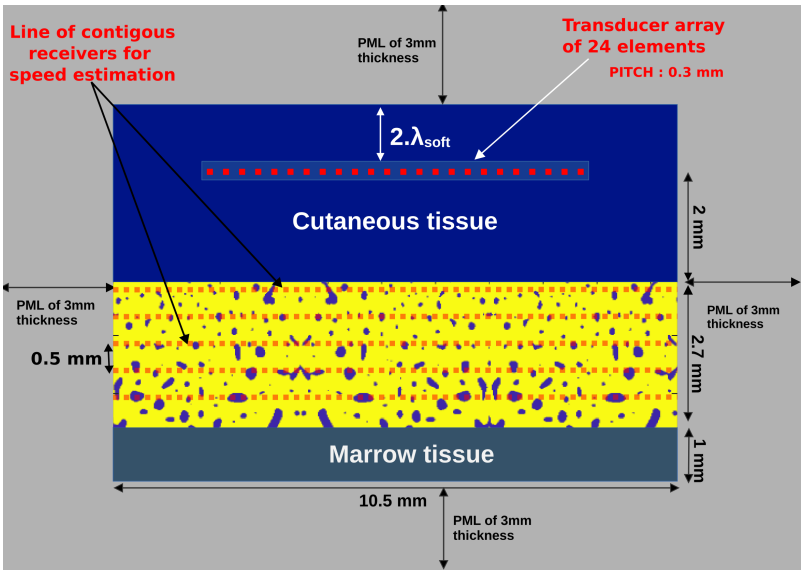

Figure B.13: Configuration model used for estimation of wave-speed in cortical bone. Virtual receivers are placed inside bone along 5 equally spaced (spacing=0.5 mm) lines (red dotted line inside cortical bone layer).

Appendix C Determination of the optimal receive f-number for endosteal detection

In order to use the DAS algorithm optimally, the receive f-number was optimized as explained by Perrot et al. [32]. The interface visibility is evaluated for 25 different f-number values ranging from 0.2 to 2.6. The f-number was constant throughout the image, resulting in a different number of elements used for each point of the image. For a f-number greater than 2.6, less than 3 elements are used for the reconstruction of the endosteal interface, therefore the f-number was studied for values lower than 2.6. For a configuration without cortical pores (Ct.Por=0%), C_{EP} (defined in section 2.6) increases with f-number and reaches its maximum for a f-number close to 1.9 (increase of 8 dB). This is illustrated in Figure C.14.

Globally, the f-number that maximizes C_{EP} is close to 1.9. This value of f-number corresponds

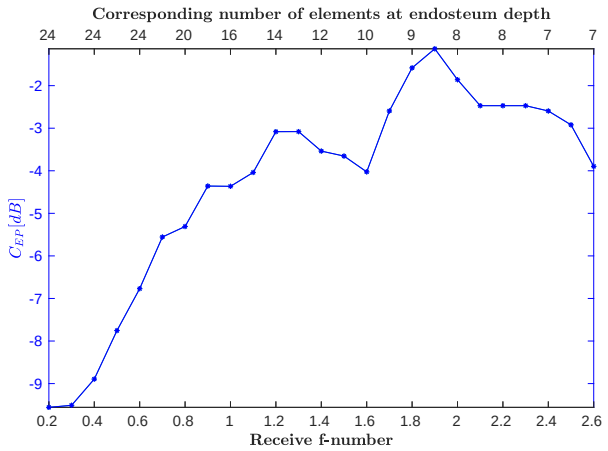

Figure C.14: Endosteum–Periosteum contrast for different values of f-number for a configuration without microstructure (i.e. porosity= 0%). The number of active elements is also given.

to a receive aperture of 2.35 mm equivalent to 9 active elements for a focusing depth of 4.7 mm (i.e at the endosteal interface). For C_{EI}, the increase of contrast is smaller (increase of 3 dB), but the tendency is the same as for C_{EP} for almost all configurations. The f-number that maximizes C_{EI} is also close to 1.9. The metrics decrease for large f-number values.

Figure C.15 is an example plot of endosteal interface visibility against f-number for a configuration with a cortical porosity of 5.5%.

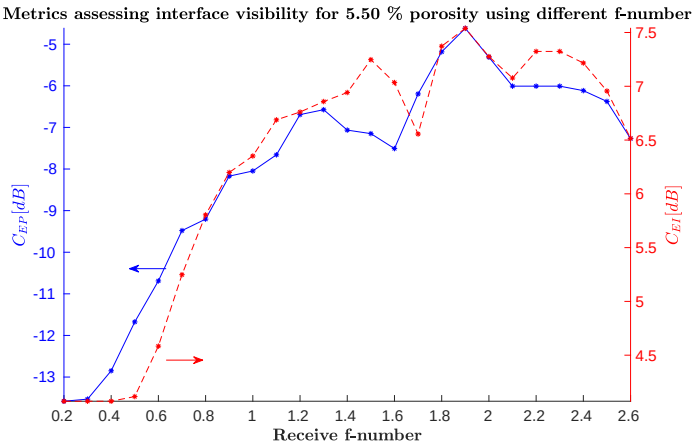

Figure C.15: Quantitative assessment of endosteal interface visibility as a function of the f-number, for a microstructure with a porosity of 5.5% porosity. The blue solid curve is relative interface contrast (C_{EP}) and the red dashed curve is endosteal interface contrast (C_{EI}).

Appendix D Power reflection coefficient at the endosteal surface.

The amplitude of the specular reflection is important to interpret the appearance of the interfaces in the images of this study. Therefore the power reflection coefficient at the endosteal surface were calculated for different microstructure. As porosity increases, the speed of sound in cortical bone decreases leading to a drop of the power reflection coefficient at endosteal interface (R_{end}). The theoretical power reflection coefficient of plane waves is:

$$R_{end} = \left(\frac{Z_{marrow} - Z_{bone}}{Z_{marrow} + Z_{bone}} \right)^2,$$

where Z_{marrow} and Z_{bone} are the impedances of marrow and bone. In Figure D.16, reports R_{end} as a function of cortical porosity. In the porosity range 2-24 %, R_{end} decreases by 25 % of its value at 2 % porosity.

Appendix E Attenuation coefficient

Estimation of the ultrasonic attenuation coefficient with numerical simulations. The attenuation value is important to interpret the ultrasound images of cortical bone obtained in this study. Therefore an analysis were conducted to document the variation of attenuation for our samples. Beside absorption inside the bone matrix, scattering due to pores contributes to the total amount of attenuation. To estimate the total attenuation coefficient in cortical bone additional simulation mimicking the substitution method commonly used for the experimental characterization of attenuation [46] were performed. For each model (i.e. each microstructure, see Figure 3), a plane wave

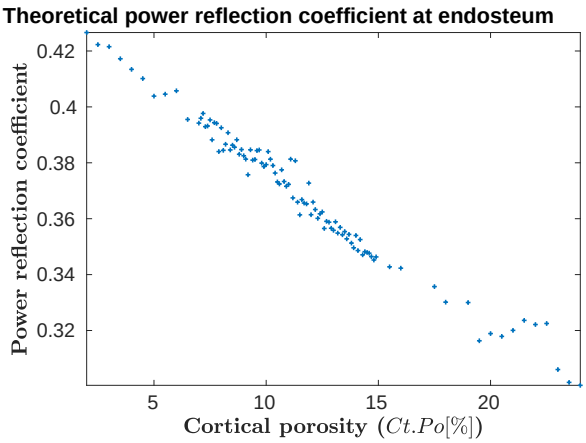

Figure D.16: Plane wave power reflection coefficient at the endosteal interface for each cortical microstructure.

at normal incidence is emitted by the transducer array and recorded after propagation through the layer of cortical bone by a line of virtual receivers positioned slightly below and parallel to the endosteal interface. To obtain a reference signal, the bone tissue is replaced with soft tissue. The attenuation coefficient in cortical bone was derived from the ratio of the magnitude spectrum of the signal received after propagation through bone ($|S(f)|$) to the magnitude spectrum of the reference signal ($|S_0(f)|$). Losses due to transmission through the two interfaces of the cortical bone layer were taken into account using the values of the plane wave transmission coefficients T_p (through the periosteal interface) and T_e (through the endosteal interface) calculated from the estimated compressional wave-speed (V_1) and apparent mass density (ρ). The attenuation coefficient α_{dB} in cortical bone expressed in dB/cm is obtained from:

$$\alpha_{dB}(f) = \frac{20}{\ln(10)} \frac{1}{Ct.Th} \ln\left(\frac{|S_0(f)|T_pT_e}{|S(f)|}\right)$$

, where Ct.Th is the thickness of the cortical bone layer in cm (0.27 cm).

Two sets of simulation were performed: with and without absorption in the bone matrix. Absorption in the bone matrix was set to 19.05 dB/cm as explained in Materials and Methods. Figure E.17 shows the obtained attenuation coefficient values as a function of porosity.

Relationship with microstructure. The difference between attenuation coefficients for simulations with and without bone matrix absorption is close to 19 dB/cm as expected. In fact, in this study, the maximum normalized frequency calculated as the product of sample wavenumber(k) and

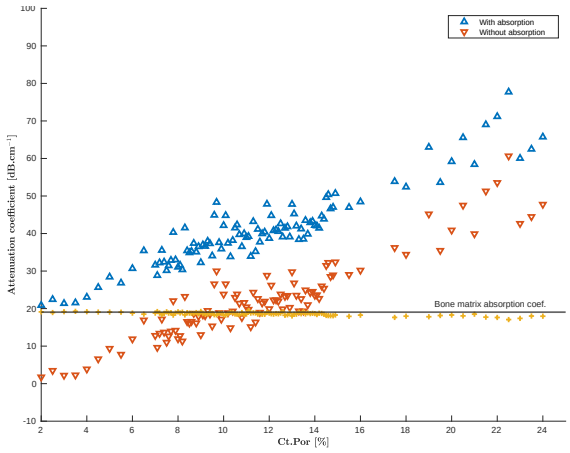

Figure E.17: Ultrasonic attenuation coefficient at 2.5 MHz in cortical bone as a function of porosity for simulations with absorption in bone matrix (blue upward pointing triangles) and simulations without absorption (red downward pointing triangles). The difference between these two data sets is also shown as yellow crosses.

sample median pore diameter (Ct.Po.Dm) is 0.66 (moderate scattering regime), therefore, total attenuation is expected to be a linear summation of the bone matrix absorption and attenuation due to scattering [25].

Scattering attenuation coefficient is highly influenced by cortical microstructure. In the porosity range (2-24 %), attenuation coefficient increased by 40 dB/cm (Figure E.17). Spearman rank

	Lg.Po.Dm	Ct.Por	Dm.DC-9	Dm.IDRng	Ct.Po.Dm	Dm.Rng	Dm.DC-1	Sm.Po.Dm	Ct.Po.Dn
Attenuation coefficient	0.92^{2}	0.89^{2}	0.83^{2}	0.82^{2}	0.70^{2}	0.67^{1}	0.54^{2}	0.46^{2}	$-0.21^{n.s}$

Table E.3: Spearman correlation coefficient r_s between attenuation coefficient and microstructure properties (see 2.2 for the definition of variables). $^{n.s}$: not significant $p > 0.05$, ^{1} : $0.001 < p < 0.05$, ^{2} : $p < 0.001$

correlation coefficient between attenuation and microstructure variables were evaluated. There was strong positive correlation coefficient (r_s) for large pore size ($r_s = 0.92$), porosity ($r_s = 0.89$) and 9^{th} decile of diameters ($r_s = 0.83$) (see Table E.3). These statistics suggest that scattering magnitude increases with pore size and is dominated by scattering caused by large pores.

Appendix F Large pore influence on the visibility of the endosteal interface

Figure F.18 illustrates pore size effect on the visibility of the endosteal interface. The SR-µCT images of microstructures correspond to the reconstructed images of Figure 10. In the leftmost image, the microstructure does not contain pores with large diameter (Lg.Po.Dm=183.3 µm) and the

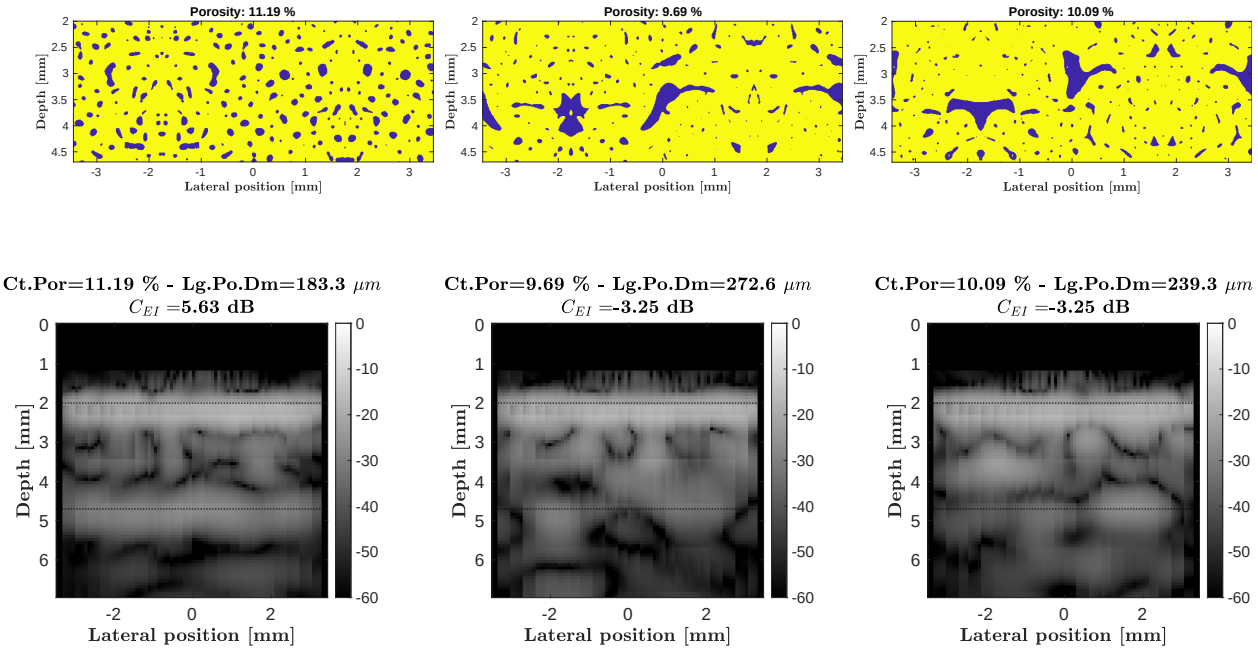

Figure F.18: Binarized SR-µCT image of microstructure with similar porosities (top) but increasing large pore size and their corresponding reconstructed ultrasound images (down).

endosteal interface is clearly visible ($C_{EI} = 5.63$ dB) while in the two following images some large pores (Lg.Po.Dm=272.6 µm and Lg.Po.Dm=239.3 µm) are observed and the endosteal interface is not visible ($C_{EI} = -3.25$ dB for both).

References

[1] C. Cooper, S. L. Ferrari, IOF Compendium of OsteoporosisPublisher: International Osteoporosis Foundation (IOF) (2017).
URL https://archive-ouverte.unige.ch/unige:125569

[2] E. S. Siris, Y.-T. Chen, T. A. Abbott, E. Barrett-Connor, P. D. Miller, L. E. Wehren, M. L. Berger, Bone Mineral Density Thresholds for Pharmacological Intervention to Prevent Fractures, Archives of Internal Medicine 164 (10) (2004) 1108–1112. doi:10.1001/archinte.164.10.1108.
URL https://doi.org/10.1001/archinte.164.10.1108

[3] K. Briot, S. Paternotte, S. Kolta, R. Eastell, D. Felsenberg, D. M. Reid, C.-C. Glüer, C. Roux, FRAX®: Prediction of Major Osteoporotic Fractures in Women from the General

Population: The OPUS Study, PLOS ONE 8 (12) (2013) e83436, publisher: Public Library of Science. doi:10.1371/journal.pone.0083436.
URL https://journals.plos.org/plosone/article?id=10.1371/journal.pone.0083436

[4] P. Laugier, Q. Grimal, Bone Quantitative Ultrasound: New Horizons, 1st Edition, no. 1364 in Advances in Experimental Medicine and Biology, Springer International Publishing, 2022.

[5] Q. Grimal, P. Laugier, Quantitative Ultrasound Assessment of Cortical Bone Properties Beyond Bone Mineral Density, IRBM 40 (1) (2019) 16–24. doi:10.1016/j.irbm.2018.10.006.
URL https://www.sciencedirect.com/science/article/pii/S1959031818301982

[6] V. Beltrame, R. Stramare, N. Rebellato, F. Angelini, A. C. Frigo, L. Rubaltelli, Sonographic evaluation of bone fractures: a reliable alternative in clinical practice?, Clinical Imaging 36 (3) (2012) 203–208. doi:10.1016/j.clinimag.2011.08.013.
URL https://www.sciencedirect.com/science/article/pii/S0899707111001732

[7] G. Renaud, P. Kruizinga, D. Cassereau, P. Laugier, In vivo ultrasound imaging of the bone cortex, Physics in Medicine & Biology 63 (12) (2018) 125010, publisher: IOP Publishing. doi:10.1088/1361-6560/aac784.
URL https://doi.org/10.1088%2F1361-6560%2Faac784

[8] H. Nguyen Minh, J. Du, K. Raum, Estimation of Thickness and Speed of Sound in Cortical Bone Using Multifocus Pulse-Echo Ultrasound, IEEE transactions on ultrasonics, ferroelectrics, and frequency control 67 (3) (2020) 568–579. doi:10.1109/TUFFC.2019.2948896.

[9] P. Augat, S. Schorlemmer, The role of cortical bone and its microstructure in bone strength, Age and Ageing 35 (suppl_2) (2006) ii27–ii31. doi:10.1093/ageing/afl081.
URL https://doi.org/10.1093/ageing/afl081

[10] Y. Bala, R. Zebaze, E. Seeman, Role of cortical bone in bone fragility, Current Opinion in Rheumatology 27 (4) (2015) 406–413. doi:10.1097/BOR.0000000000000183.
URL https://journals.lww.com/co-rheumatology/Abstract/2015/07000/Role_of_cortical_bone_in_bone_fragility.13.aspx

[11] K. L. Bell, N. Loveridge, J. Power, N. Garrahan, B. F. Meggitt, J. Reeve, Regional differences in cortical porosity in the fractured femoral neck, Bone 24 (1) (1999) 57–64. doi:10.1016/S8756-3282(98)00143-4.
URL https://www.sciencedirect.com/science/article/pii/S8756328298001434

[12] C. M. Andreasen, J.-M. Delaisse, B. C. van der Eerden, J. P. van Leeuwen, M. Ding, T. L. Andersen, Understanding Age-Induced Cortical Porosity in Women: The Accumulation and Coalescence of Eroded Cavities Upon Existing Intracortical Canals Is the Main Contributor, Journal of Bone and Mineral Research 33 (4) (2018) 606–620, _eprint: https://onlinelibrary.wiley.com/doi/pdf/10.1002/jbmr.3354. doi:10.1002/jbmr.3354.
URL https://onlinelibrary.wiley.com/doi/abs/10.1002/jbmr.3354

[13] V. Bousson, A. Meunier, C. Bergot, E. Vicaut, M. A. Rocha, M. H. Morais, A.-M. Laval-Jeantet, J.-D. Laredo, Distribution of Intracortical Porosity in Human Midfemoral Cortex by Age and Gender, Journal of Bone and Mineral Research 16 (7) (2001) 1308–1317. doi:10.1359/jbmr.2001.16.7.1308.
URL https://onlinelibrary.wiley.com/doi/abs/10.1359/jbmr.2001.16.7.1308

[14] D. M. L. Cooper, C. D. L. Thomas, J. G. Clement, A. L. Turinsky, C. W. Sensen, B. Hallgrímsson, Age-dependent change in the 3D structure of cortical porosity at the human femoral midshaft, Bone 40 (4) (2007) 957–965. doi:10.1016/j.bone.2006.11.011.
URL https://www.sciencedirect.com/science/article/pii/S8756328206008465

[15] C. Chappard, S. Bensalah, C. Olivier, P. J. Gouttenoire, A. Marchadier, C. Benhamou, F. Peyrin, 3D characterization of pores in the cortical bone of human femur in the elderly at different locations as determined by synchrotron micro-computed tomography images, Osteoporosis international: a journal established as result of cooperation between the European Foundation for Osteoporosis and the National Osteoporosis Foundation of the USA 24 (3) (2013) 1023–1033. doi:10.1007/s00198-012-2044-4.

[16] K. Raum, I. Leguerney, F. Chandelier, M. Talmant, A. Saïed, F. Peyrin, P. Laugier, Site-matched assessment of structural and tissue properties of cortical bone using scanning acoustic microscopy and synchrotron radiation $\upmu$CT, Physics in Medicine and Biology 51 (3)

(2006) 733–746, publisher: IOP Publishing. doi:10.1088/0031-9155/51/3/017.
URL https://doi.org/10.1088/0031-9155/51/3/017

[17] M. S. Stein, S. A. Feik, C. D. L. Thomas, J. G. Clement, J. D. Wark, An Automated Analysis of Intracortical Porosity in Human Femoral Bone Across Age, Journal of Bone and Mineral Research 14 (4) (1999) 624–632, _eprint: https://onlinelibrary.wiley.com/doi/pdf/10.1359/jbmr.1999.14.4.624. doi:10.1359/jbmr.1999.14.4.624.
URL https://onlinelibrary.wiley.com/doi/abs/10.1359/jbmr.1999.14.4.624

[18] O. Yousefian, R. D. White, Y. Karbalaeisadegh, H. T. Banks, M. Muller, The effect of pore size and density on ultrasonic attenuation in porous structures with mono-disperse random pore distribution: A two-dimensional in-silico study, The Journal of the Acoustical Society of America 144 (2) (2018) 709. doi:10.1121/1.5049782.

[19] M. P. Zamorani, M. Valle, Bone and Joint, in: S. Bianchi, C. Martinoli (Eds.), Ultrasound of the Musculoskeletal System, Medical Radiology, Springer, Berlin, Heidelberg, 2007, pp. 137–185. doi:10.1007/978-3-540-28163-4_5.
URL https://doi.org/10.1007/978-3-540-28163-4_5

[20] X. Cai, H. Follet, L. Peralta, M. Gardegaront, D. Farlay, R. Gauthier, B. Yu, E. Gineyts, C. Olivier, M. Langer, A. Gourrier, D. Mitton, F. Peyrin, Q. Grimal, P. Laugier, Anisotropic elastic properties of human femoral cortical bone and relationships with composition and microstructure in elderly, Acta Biomaterialia 90 (2019) 254–266. doi:10.1016/j.actbio.2019.03.043.
URL https://www.sciencedirect.com/science/article/pii/S1742706119302181

[21] X. Cai, R. Brenner, L. Peralta, C. Olivier, P.-J. Gouttenoire, C. Chappard, F. Peyrin, D. Cassereau, P. Laugier, Q. Grimal, Homogenization of cortical bone reveals that the organization and shape of pores marginally affect elasticity, Journal of The Royal Society Interface 16 (151) (2019) 20180911, publisher: Royal Society. doi:10.1098/rsif.2018.0911.
URL https://royalsocietypublishing.org/doi/10.1098/rsif.2018.0911

[22] C. M. Moran, N. L. Bush, J. C. Bamber, Ultrasonic propagation properties of excised human skin, Ultrasound in Medicine & Biology 21 (9) (1995) 1177–1190. doi:10.1016/

0301-5629(95)00049-6.
URL https://www.sciencedirect.com/science/article/pii/0301562995000496

[23] S. Kawasaki, R. Ueda, A. Hasegawa, A. Fujita, T. Mihata, M. Matsukawa, M. Neo, Ultrasonic wave properties of human bone marrow in the femur and tibia, The Journal of the Acoustical Society of America 138 (1) (2015) EL83–EL87. doi:10.1121/1.4922764.
URL https://asa.scitation.org/doi/10.1121/1.4922764

[24] R. Lakes, H. S. Yoon, J. Lawrence Katz, Ultrasonic wave propagation and attenuation in wet bone, Journal of Biomedical Engineering 8 (2) (1986) 143–148. doi:10.1016/0141-5425(86)90049-X.
URL https://www.sciencedirect.com/science/article/pii/014154258690049X

[25] O. Yousefian, Y. Karbalaeisadegh, M. Muller, Frequency-dependent analysis of ultrasound apparent absorption coefficient in multiple scattering porous media: application to cortical bone, Physics in Medicine & Biology 66 (3) (2021) 035026. doi:10.1088/1361-6560/abb934.
URL https://doi.org/10.1088/1361-6560/abb934

[26] K. Mohanty, O. Yousefian, Y. Karbalaeisadegh, M. Ulrich, Q. Grimal, M. Muller, Artificial neural network to estimate micro-architectural properties of cortical bone using ultrasonic attenuation: A 2-D numerical study, Computers in Biology and Medicine 114 (2019) 103457. doi:10.1016/j.compbiomed.2019.103457.
URL http://www.sciencedirect.com/science/article/pii/S0010482519303312

[27] Y. Karbalaeisadegh, O. Yousefian, G. Iori, K. Raum, M. Muller, Acoustic diffusion constant of cortical bone: Numerical simulation study of the effect of pore size and pore density on multiple scattering, The Journal of the Acoustical Society of America 146 (2) (2019) 1015–1023, publisher: Acoustical Society of America. doi:10.1121/1.5121010.
URL https://asa.scitation.org/doi/10.1121/1.5121010

[28] E. Bossy, SimSonic: free fdtd software for the simulation of ultrasonic waves propagation.
URL http://www.simsonic.fr/

[29] E. Bossy, F. Padilla, F. Peyrin, P. Laugier, Three-dimensional simulation of ultrasound propagation through trabecular bone structures measured by synchrotron microtomography, Physics in Medicine and Biology 50 (23) (2005) 5545–5556, publisher: IOP Publishing.

555 doi:10.1088/0031-9155/50/23/009.
556 URL https://doi.org/10.1088%2F0031-9155%2F50%2F23%2F009

557 [30] E. Bossy, Q. Grimal, Numerical Methods for Ultrasonic Bone Characterization, in: P. Laugier,
558 G. Haïat (Eds.), Bone Quantitative Ultrasound, Springer Netherlands, Dordrecht, 2011, pp.
559 181–228. doi:10.1007/978-94-007-0017-8_8.
560 URL https://doi.org/10.1007/978-94-007-0017-8_8

561 [31] Q. Grimal, K. Raum, A. Gerisch, P. Laugier, A determination of the minimum sizes of repre-
562 sentative volume elements for the prediction of cortical bone elastic properties, Biomechanics
563 and Modeling in Mechanobiology 10 (6) (2011) 925–937. doi:10.1007/s10237-010-0284-9.
564 URL https://doi.org/10.1007/s10237-010-0284-9

565 [32] V. Perrot, M. Polichetti, F. Varray, D. Garcia, So you think you can DAS? A viewpoint on
566 delay-and-sum beamforming, Ultrasonics 111 (2021) 106309. doi:10.1016/j.ultras.2020.
567 106309.
568 URL https://www.sciencedirect.com/science/article/pii/S0041624X20302444

569 [33] X. Cai, L. Peralta, R. Brenner, G. Iori, D. Cassereau, K. Raum, P. Laugier, Q. Gri-
570 mal, Anisotropic elastic properties of human cortical bone tissue inferred from inverse ho-
571 mogenization and resonant ultrasound spectroscopy, Materialia 11 (2020) 100730. doi:
572 10.1016/j.mtla.2020.100730.
573 URL https://www.sciencedirect.com/science/article/pii/S2589152920301472

574 [34] L. Peralta, J. D. Maeztu Redin, F. Fan, X. Cai, P. Laugier, J. Schneider, K. Raum, Q. Gri-
575 mal, Bulk wave velocities in cortical bone reflect porosity and compression strength, Ultra-
576 sound in Medicine & Biology 47 (3) (2021) 799–808. doi:https://doi.org/10.1016/j.
577 ultrasmedbio.2020.11.012.
578 URL https://www.sciencedirect.com/science/article/pii/S0301562920305202

579 [35] G. Iori, J. Schneider, A. Reisinger, F. Heyer, L. Peralta, C. Wyers, M. Gräsel, R. Barkmann,
580 C. C. Glüer, J. P. v. d. Bergh, D. Pahr, K. Raum, Large cortical bone pores in the tibia
581 are associated with proximal femur strength, PLOS ONE 14 (4) (2019) e0215405, publisher:
582 Public Library of Science. doi:10.1371/journal.pone.0215405.

URL https://journals.plos.org/plosone/article?id=10.1371/journal.pone.0215405

[36] G. Iori, J. Du, J. Hackenbeck, V. Kilappa, K. Raum, Estimation of Cortical Bone Microstructure from Ultrasound Backscatter, IEEE Transactions on Ultrasonics, Ferroelectrics, and Frequency Control (2020) 1–1Conference Name: IEEE Transactions on Ultrasonics, Ferroelectrics, and Frequency Control. doi:10.1109/TUFFC.2020.3033050.

[37] Q. Grimal, D. Rohrbach, J. Grondin, R. Barkmann, C.-C. Glüer, K. Raum, P. Laugier, Modeling of Femoral Neck Cortical Bone for the Numerical Simulation of Ultrasound Propagation, Ultrasound in Medicine & Biology 40 (5) (2014) 1015–1026. doi:10.1016/j.ultrasmedbio.2013.11.010.
URL https://linkinghub.elsevier.com/retrieve/pii/S0301562913011538

[38] D. M. L. Cooper, C. E. Kawalilak, K. Harrison, B. D. Johnston, J. D. Johnston, Cortical Bone Porosity: What Is It, Why Is It Important, and How Can We Detect It?, Current Osteoporosis Reports 14 (5) (2016) 187–198. doi:10.1007/s11914-016-0319-y.
URL https://doi.org/10.1007/s11914-016-0319-y

[39] Q. Grimal, M. Talmant, G. Renaud, Measurement of ultrasonic anisotropic attenuation of P-wave in millimetric-sized human cortical bone samples [abstract], International Symposium on Ultrasonic Characterisation of Bone (2019, Villa-Clythia, Fréjus, France) 1.

[40] R. M. Zebaze, A. Ghasem-Zadeh, A. Bohte, S. Iuliano-Burns, M. Mirams, R. I. Price, E. J. Mackie, E. Seeman, Intracortical remodelling and porosity in the distal radius and post-mortem femurs of women: a cross-sectional study, The Lancet 375 (9727) (2010) 1729–1736. doi:10.1016/S0140-6736(10)60320-0.
URL https://www.sciencedirect.com/science/article/pii/S0140673610603200

[41] G. Armbrecht, H. Nguyen Minh, J. Massmann, K. Raum, Pore-Size Distribution and Frequency-Dependent Attenuation in Human Cortical Tibia Bone Discriminate Fragility Fractures in Postmenopausal Women With Low Bone Mineral Density, JBMR Plus 5 (11) (2021) e10536. doi:10.1002/jbm4.10536.
URL https://onlinelibrary.wiley.com/doi/abs/10.1002/jbm4.10536

[42] H. Hasegawa, Recent Developments in Adaptive Beamforming, in: 2019 IEEE International Ultrasonics Symposium (IUS), 2019, pp. 1063–1066, iSSN: 1948-5727. doi:10.1109/ULTSYM.2019.8925830.

[43] A. Rodriguez-Molares, A. Fatemi, L. Løvstakken, H. Torp, Specular Beamforming, IEEE Transactions on Ultrasonics, Ferroelectrics, and Frequency Control 64 (9) (2017) 1285–1297, conference Name: IEEE Transactions on Ultrasonics, Ferroelectrics, and Frequency Control. doi:10.1109/TUFFC.2017.2709038.

[44] R. Lavarello, F. Kamalabadi, W. O'Brien, A regularized inverse approach to ultrasonic pulse-echo imaging, IEEE Transactions on Medical Imaging 25 (6) (2006) 712–722, conference Name: IEEE Transactions on Medical Imaging. doi:10.1109/TMI.2006.873297.

[45] S. Liu, Y. Wang, X. Yang, B. Lei, L. Liu, S. X. Li, D. Ni, T. Wang, Deep Learning in Medical Ultrasound Analysis: A Review, Engineering 5 (2) (2019) 261–275. doi:10.1016/j.eng.2018.11.020.
URL https://www.sciencedirect.com/science/article/pii/S2095809918301887

[46] M. Sasso, G. Haïat, Y. Yamato, S. Naili, M. Matsukawa, Frequency Dependence of Ultrasonic Attenuation in Bovine Cortical Bone: An In Vitro Study, Ultrasound in Medicine & Biology 33 (12) (2007) 1933–1942. doi:10.1016/j.ultrasmedbio.2007.05.022.
URL https://www.sciencedirect.com/science/article/pii/S0301562907002724